CrossMark

# $Ba_{6-3x}Nd_{8+2x}Ti_{18}O_{54}$ Tungsten Bronze: A New High-Temperature $n$-Type Oxide Thermoelectric

FERIDOON AZOUGH,[1,8] ROBERT FREER,[1] STEPHEN R. YEANDEL,[2]
JAKUB D. BARAN,[2] MARCO MOLINARI,[2] STEPHEN C. PARKER,[2]
EMMANUEL GUILMEAU,[3] DEMIE KEPAPTSOGLOU,[4] QUENTIN
RAMASSE,[4] ANDY KNOX,[5] DUNCAN GREGORY,[5] DOUGLAS PAUL,[5]
MANOSH PAUL,[5] ANDREA MONTECUCCO,[5] JONATHAN SIVITER,[5]
PAUL MULLEN,[5] WENGUAN LI,[5] GUANG HAN,[5] ELENA A. MAN,[5]
HASAN BAIG,[6] TAPAS MALLICK,[6] NAZMI SELLAMI,[6] GAO MIN,[7] and
TRACY SWEET[7]

1.—University of Manchester, Manchester, UK. 2.—University of Bath, Bath, UK. 3.—Laboratoire CRISMAT, Caen, France. 4.—SuperSTEM Laboratory, Daresbury, UK. 5.—University of Glasgow, Glasgow, UK. 6.—Exeter University, Exeter, UK. 7.—Cardiff University, Cardiff, UK. 8.—e-mail: feridoon.azough@manchester.ac.uk

Semiconducting $Ba_{6-3x}Nd_{8+2x}Ti_{18}O_{54}$ ceramics (with $x = 0.00$ to $0.85$) were synthesized by the mixed oxide route followed by annealing in a reducing atmosphere; their high-temperature thermoelectric properties have been investigated. In conjunction with the experimental observations, atomistic simulations have been performed to investigate the anisotropic behavior of the lattice thermal conductivity. The ceramics show promising $n$-type thermoelectric properties with relatively high Seebeck coefficient, moderate electrical conductivity, and temperature-stable, low thermal conductivity; For example, the composition with $x = 0.27$ (i.e., $Ba_{5.19}Nd_{8.54}Ti_{18}O_{54}$) exhibited a Seebeck coefficient of $S_{1000K} = 210$ $\mu$V/K, electrical conductivity of $\sigma_{1000K} = 60$ S/cm, and thermal conductivity of $k_{1000K} = 1.45$ W/(m K), leading to a $ZT$ value of $0.16$ at 1000 K.

**Key words:** Oxide ceramic, tungsten bronze, titanate, thermal conductivity, thermoelectric, molecular dynamics, modelling

## INTRODUCTION

Thermoelectric energy conversion is widely recognized as a promising technology for both electric power generation in terms of waste heat recovery and cooling of various electronic devices.[1]

An efficient thermoelectric material should possess thermal properties similar to those of glass and electrical properties similar to those of perfect single-crystal material, i.e., poor thermal conductivity with good electrical conductivity. Metal oxides are among the current candidates because of their stability at high temperatures, abundance, and low toxicity.[2] The perovskite-structured $SrTiO_3$ has

been at the center of recent development of $n$-type high-temperature thermoelectric ceramics and has shown good electrical conductivity, $\sigma$, and high Seebeck coefficient, $S$, yielding power factors $S^2\sigma \leq 3.5$ mW/K m in single-crystal form.[3] However, the overall performance of polycrystalline ceramics for commercial applications is compromised by large thermal conductivity,[4] $k = 8$ W/(m K) to 3 W/(m K), which reduces the thermoelectric figure of merit, $ZT = (S^2\sigma/k)T$, where $T$ is the absolute temperature. Recently, it has been shown that tungsten bronze compounds such as $Sr_{1-x}Ba_xNb_2O_6$ are potential candidates for high-temperature applications.[5–7] These materials exhibit low thermal conductivity due to the presence of different sublattices occupied by different species, and unoccupied lattice sites which are too small to

accommodate the constituent elements. Low thermal conductivity of 1.5 W/(m K) was reported for bulk $Sr_{1-x}Ba_xNb_2O_6$ material, with an even lower value of 0.6 W/(m K) along the $c$-direction due to crystallographic anisotropy.

For many years, $Ba_{6-3x}Nd_{8+2x}Ti_{18}O_{54}$ tungsten bronze ceramics have been investigated with regards to their crystal structure and dielectric properties.[8–10] They crystallize in a tungsten-bronze-type structure with orthorhombic symmetry with $a$ = 24.2 Å, $b$ = 7.7 Å, and $c$ = 12.2 Å in space group $Pnma$. The basic structure is a tungsten-bronze-type framework formed by corner-sharing $TiO_6$ octahedra; the structure is characterized by distorted tetragonal and pentagonal tunnels running parallel to the $c$-axis. The pentagonal sites are occupied by Ba, and the tetragonal sites are occupied by Nd. At higher levels of Ba, the excess Ba shares the tetragonal sites with Nd. In this study, we investigated the high-temperature thermoelectric properties of tungsten bronze $Ba_{6-3x}Nd_{8+2x}Ti_{18}O_{54}$ ceramics. To conduct the first assessment of the thermoelectric properties of $Ba_{6-3x}Nd_{8+2x}Ti_{18}O_{54}$ tungsten bronze, the two end-members, with $x$ = 0.0 and $x$ = 0.85, and an intermediate composition with $x$ = 0.27 were selected. The intermediate composition $x$ = 0.27 was chosen because it marks the onset of change in the dielectric loss (closely related to the resistivity) in the system.[11]

## EXPERIMENTAL PROCEDURES

Ceramic samples of $Ba_{6-3x}Nd_{8+2x}Ti_{18}O_{54}$ ($x$ = 0.0 denoted as X0, $x$ = 0.27 denoted as X27, and $x$ = 0.85 denoted as X85) were prepared by the conventional mixed oxide route. Starting materials were high-purity powders of $BaCO_3$ (Solvay, 99.5%), $SrCO_3$ (Solvay, 99.5%), $Nd_2O_3$ (Sigma Aldrich, 99.9%) and $TiO_2$ (Tioxide UK, 99.9%). The powders were weighed in batches according to the required formulations and wet milled for 24 h in a vibratory mill using zirconia balls and propan-2-ol. The powders were then dried at 85°C for 24 h and calcined at 1100°C for 4 h. The calcined powders were attrition milled using zirconia balls and propan-2-ol. Powders were uniaxially compacted into pellets of 20 mm diameter and 5 mm thickness at pressure of 50 MPa prior to sintering at 1400°C to 1450°C for 4 h in air. The sintered samples were subsequently annealed at 1400°C for 12 h in 5% $H_2$–95% Ar.

The products were ground and polished by standard techniques to make them ready for microstructure observations. After carbon coating, the microstructures were examined by scanning electron microscopy using a Philips XL30 FEGSEM equipped with energy-dispersive spectroscopy capability.

Samples for transmission electron microscopy (TEM) and scanning transmission electron microscopy (STEM) investigation were prepared by both ion-beam thinning and crushing techniques. Structures were initially investigated by selected-area electron diffraction (SAED) and high-resolution transmission electron microscopy (HRTEM) techniques using a FEI FEGTEM (Tecnai G2, Hillsboro, OR) operating at 300 kV. Subsequently, atomic-level-resolution structural characterization was carried out using an aberration-corrected Nion STEM (UltraSTEM™ 100; Nion Company, Kirkland, WA) located at the Daresbury SuperSTEM Laboratory, UK.

The Seebeck coefficient and electrical conductivity were measured simultaneously using a ULVAC ZEM-3 in helium atmosphere. The thermal conductivity was obtained by measuring the density (by Archimedes method), thermal diffusivity (using a built-in-house facility in argon atmosphere), and heat capacity (using a Netzsch STA 449C in nitrogen atmosphere). The thermoelectric properties were measured parallel to the pressing direction to minimize the effect of texturing.

## COMPUTATIONAL WORK

The thermal conductivity was evaluated by potential-based molecular dynamics simulations using the LAMMPS code[11] on a 20,640-atom unit simulation cell of $Ba_{6-3x}Nd_{8+2x}Ti_{18}O_{54}$ ($x$ = 0). The potential model developed by Teter was employed.[12] The simulation cell was a $3 \times 8 \times 5$ expansion of the optimized structure [23.1927 Å $\times$ 7.6912 Å $\times$ 12.2747 Å ($\alpha = \beta = \gamma = 90°$), which compares well with experimental findings], where randomly distributed $Ba'_{Nd}$ defects were introduced on tetragonal tunnels. The simulation cell was relaxed in the isothermal–isobaric ensemble [$NPT$—constant number of particles ($N$), temperature ($T$), and pressure ($P$)] at 227°C until the fluctuation of the volume was minimized, followed by a 20-ns simulation with time step of 1 fs in the canonical ensemble [$NVT$—constant number of particles ($N$), volume ($V$), and temperature ($T$)], to calculate the thermal conductivity using the Green–Kubo method.[13,14] The heat flux of the system was calculated at intervals of 10 time steps over the 20-ns simulation and then correlated at each time interval. The correlations were integrated in each dimension to yield thermal conductivities as a function of integral length. The configuration was made by using the METADISE code.[15]

## RESULTS

All ceramics were of high density, exhibiting at least 95% of theoretical density. The microstructures were characterized by bar-shaped grains with faceted faces (Fig. 1). The average length of the bars increased from typically 5 $\mu$m to 12 $\mu$m as the Nd/Ba ratio increased with composition. All products were single phase except for the composition X0, which showed minor amounts of a secondary phase in the form of enlarged platelets. Upon annealing in a reducing atmosphere, the morphology of the grains remained the same, but formation of pores and

particles in the centers of grains became evident (Fig. 2). Details of the particles are presented in the following section. A representative backscattered electron (BSE) image for sample X27 is shown in Fig. 2.

X-ray analysis confirmed that all the samples crystallized in the tungsten bronze structure after sintering in air[10,16] and the structure remained stable after annealing in the reducing atmosphere; For example, the x-ray diffraction spectra for composition X27 sintered in air and annealed in 5% $H_2$-95% Ar atmosphere are presented in Fig. 3. The x-ray spectra for both samples are very similar and represent a single-phase ceramic. The degree of texturing resulting from the bar-shaped grains can be monitored by the intensity of (002) peak. In highly oriented samples, this peak will be the highest intensity peak (unpublished data). The low intensity of the (002) peak in both air-sintered and annealed samples suggests a low degree of texturing in the samples (Fig. 3). However, as highlighted in "Experimental Procedures" section, the thermoelectric properties were measured parallel to the pressing direction to minimize the effect of texturing.

TEM studies were performed to confirm the stability of the tungsten bronze structure after annealing in the reducing atmosphere and to gain insight into the nature of the subgrain features observed by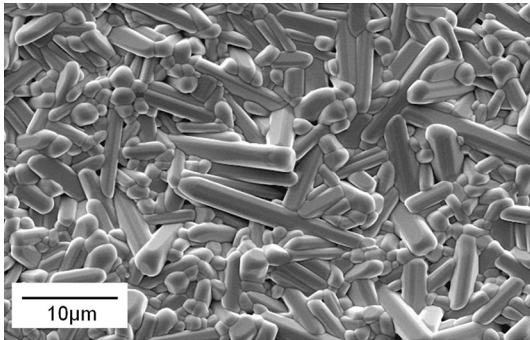 SEM. A high-resolution transmission electron microscopy (HRTEM) image for a grain in composition X0 is shown in Fig. 4. The electron diffraction pattern for the grain is shown as an inset in the bottom-right corner of the image. The electron diffraction pattern can be indexed as a [001] diffraction pattern for $Ba_{6-3x}Nd_{8+2x}Ti_{18}O_{54}$ tungsten bronze,[10] confirming the stability of the ceramic after annealing in the reduced atmosphere. Similar TEM data were obtained for compositions X27 and X85.

An atomically resolved [001] high-angle annular dark-field (HAADF) image for a grain in sample X0 annealed at 1400°C for 12 h is shown in Fig. 5a. The Z-contrast image provides direct atomic evidence of the structural model[10] shown in Fig. 5b. The HAADF image consists of spots of three different intensities (representing different types of atomic columns): the bright columns represent Ba and Nd, the lower-intensity columns are Ti, and the dark regions are columns of vacant sites in the tungsten bronze structure. The HAADF image comprises V-



Fig. 1. Representative SEM image of sintered surface for $Ba_{6-3x}Nd_{8+2x}Ti_{18}O_{54}$ ceramic.
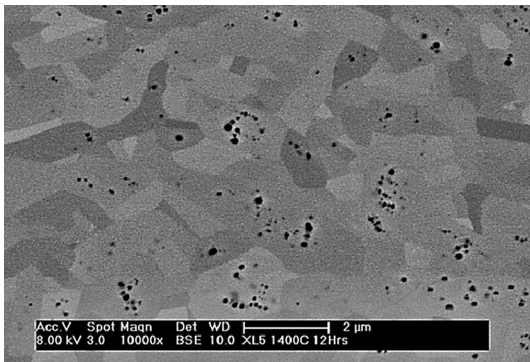


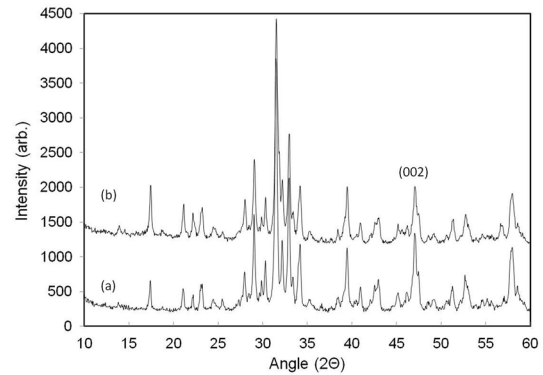Fig. 2. Backscattered SEM image for sample X27 annealed at 1400°C for 12 h in 5% $H_2$-95% Ar.



Fig. 3. X-ray diffraction spectra for composition X27: (a) sintered in air, (b) sintered in air then annealed in 5% $H_2$-95% Ar.
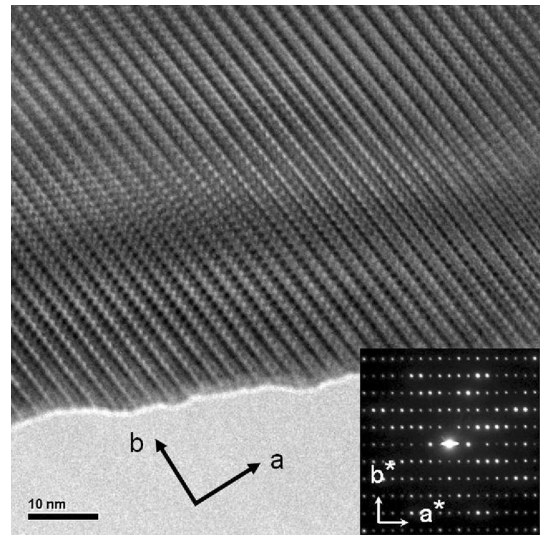


Fig. 4. HRTEM [001] image for the center part of the X0 grain annealed at 1400°C for 12 h. An electron diffraction pattern for the grain is shown as an inset in the bottom-right corner of the image.
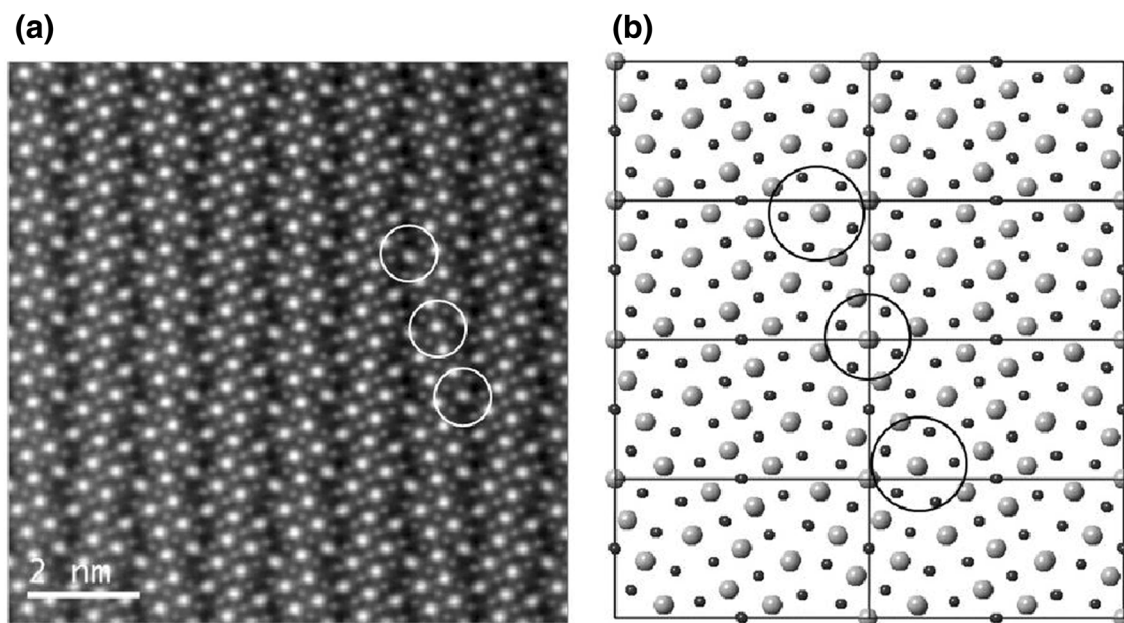
Fig. 5. (a) [001] high-angle annular dark-field (HAADF) image for a grain in sample X0 annealed at 1400°C for 12 h; (b) schematic representation of the structural model.
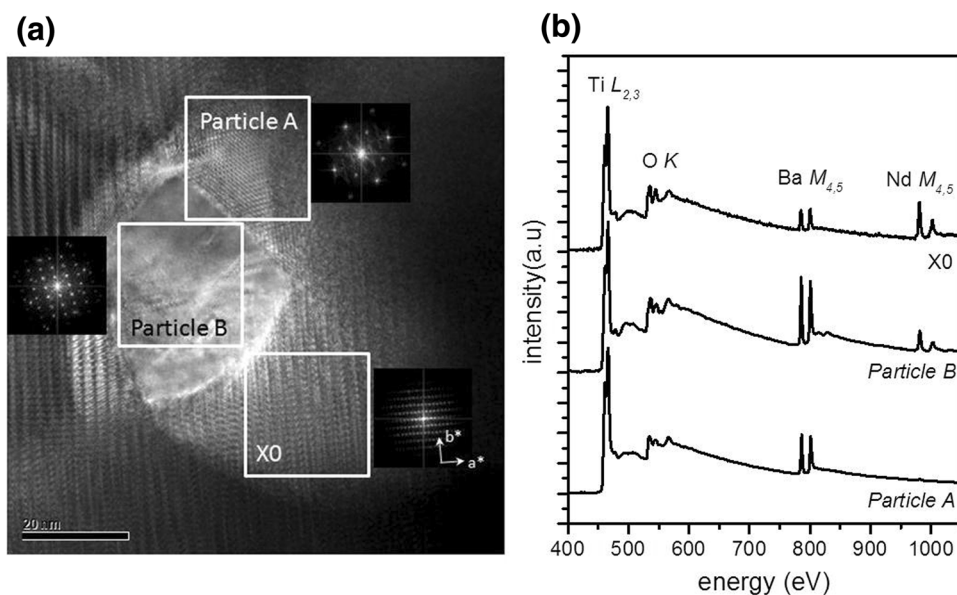


Fig. 6. HRTEM–EELS data for X0 annealed at 1400°C for 12 h: (a) HRTEM [001] image for the center part of a grain showing two particles with different image contrast and different FFT, (b) EELS spectra showing Ti-L$_{2,3}$, O-K, Ba-M$_{4,5}$, and Nd-M$_{4,5}$ for the matrix phase, X0, and the particles.

shaped rows containing seven atomic columns in each row. The pentagonal tunnels are at the end of each row, and five tetragonal tunnels are in between the pentagonal tunnels. The pentagonal and tetragonal sites are circled in Fig. 5a and b.

An HRTEM [001] image for the center part of the X0 grain annealed at 1400°C for 12 h is shown in Fig. 6a. The fast Fourier transform (FFT) for different areas of the image is shown next to the corresponding area (white squares). The FFT from the matrix is consistent with the [001] diffraction pattern for the tungsten bronze structure, as shown in the inset of Fig. 4. From the FFTs, it can be seen that two particles with different structures formed on annealing in the reducing atmosphere. Electron energy-loss spectroscopy (EELS) chemical analysis showed that particle A was composed of Ba and Ti while particle B was also mainly composed of Ba
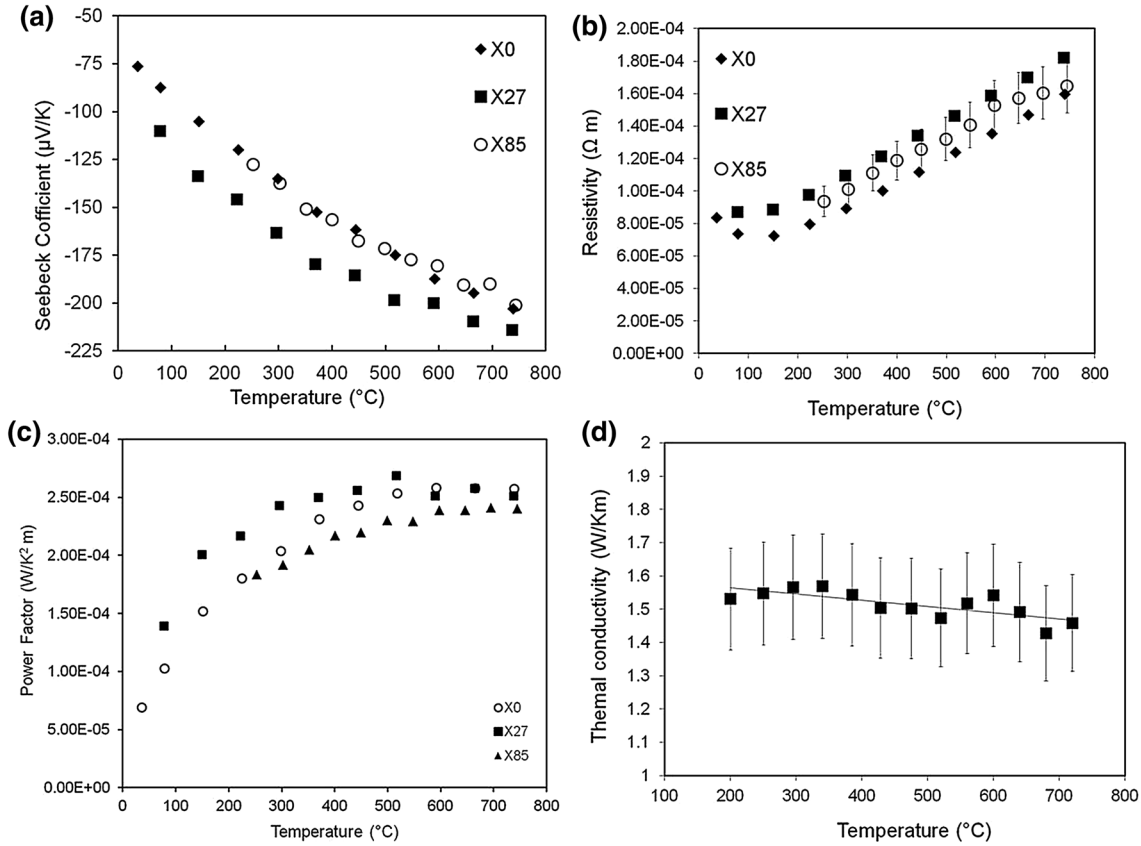
Fig. 7. Thermoelectric data for $Ba_{6-3x}Nd_{8+2x}Ti_{18}O_{54}$ ceramics as a function of temperature: (a) Seebeck coefficient for X0, X27, and X85; (b) electrical resistivity for X0, X27, and X85; (c) power factor for X0, X27, and X85; (d) thermal conductivity for X27.

**Table I. Calculated lattice thermal conductivity for the three lattice directions**

| Lattice direction | a-Axis | b-Axis | c-Axis |
|---|---|---|---|
| Lattice thermal conductivity [W/(m K)] | 1.69 | 2.49 | 1.99 |

and Ti with a small amount of Nd (Fig. 6b). Detailed, atomically resolved structural and chemical analyses of these particles are underway and will appear elsewhere.

The mechanism for the formation of nanosize pores and precipitates within the grains on annealing in the reducing atmosphere is not yet known; detailed investigation is required. However, the size of the nanopores and secondary phases formed within the grains ranges between 20 nm and 50 nm. It is therefore believed that these nanosize features may have a beneficial effect on reducing the thermal conductivity due to phonon scattering.[17,18]

The thermoelectric properties as a function of temperature for samples annealed at 1400°C for 12 h are shown in Fig. 7. The Seebeck coefficient for all three compositions reduced with increasing temperature, with no evidence of any anomaly (Fig. 7a). The absolute values of the Seebeck
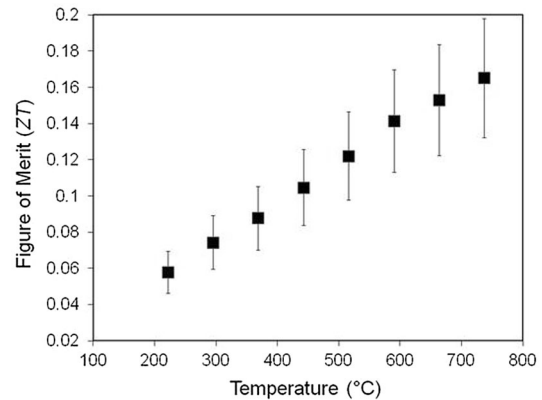


Fig. 8. Figure of merit (ZT) versus temperature for composition X27.

coefficient were highest for X0, ranging from 95 $\mu$V/K to 210 $\mu$V/K. The Seebeck coefficients for the two end-members (X0 and X85) were similar. The electrical resistivity ranged from $7 \times 10^{-5}$ $\Omega$ m to $1.8 \times 10^{-5}$ $\Omega$ m, with metallic conduction behavior above 300°C (Fig. 7b). The power factor was similar for all three compositions (Fig. 7c), being in the range of $2.0 \times 10^{-4}$ W/K²-m to $2.5 \times 10^{-4}$ W/K²-m at temperatures above 400°C. Interestingly, the thermal conductivity showed a linear dependence as a function of temperature (Fig. 7d). The

thermal conductivity values [1.57 W/(m K) to 1.43 W/(m K)] are amongst the lowest reported for an oxide thermoelectric. This thermal conduction behavior (almost glass like) probably relates to the complex crystal structure (i.e., presence of ångström-size tunnels of vacant sites for two different sublattice tunnels).

Based on established structural models[10,19] of $Ba_{6-3x}Nd_{8+2x}Ti_{18}O_{54}$ when the ceramics are fabricated in air atmosphere, the composition X0 is chemically neutral and does not have any cation vacancies in the structure; the excess Ba after filling the pentagonal channels of the structure will share the tetragonal tunnels with Nd. By increasing the value of $x$ to 0.27 and up to 0.66 (i.e., increasing the Nd content), cation vacancies will be generated at the tetragonal sites, and again the excess Ba will share tetragonal sites with Nd. Further increase of the $x$ value to above 0.66 leads to Ba deficiency; cation vacancies will be generated in the pentagonal tunnels, and all the tetragonal sites will be fully filled with Nd. This enormous variation in the distribution of Ba and Nd cations and cation vacancies within the different lattice sites, along with the formation of $Ti^{3+}$ and oxygen vacancies on annealing in the reducing atmosphere, makes it difficult to make simple direct correlations between the thermoelectric properties as a function of composition. Detailed high-resolution x-ray diffraction and advanced atomic-level electron microscopy and analysis are in progress to define this relationship.

The total lattice thermal conductivity at 227°C was calculated using potential-based molecular dynamics to be 2.05 W/(m K) for $Ba_{6-3x}Nd_{8+2x}Ti_{18}O_{54}$ ($x = 0$). This is in satisfactory agreement with the experimental data reported in Fig. 7d [approximately 1.6 W/(m K)] for the composition $x = 0.27$. Recognizing the potential anisotropy in the properties, we were able, by simulation, to separate the contribution of each direction to the average lattice thermal conductivity. We found that the lattice thermal conductivity is highly anisotropic (Table I), with the $X$-component ($a$ direction) showing the lowest value of 1.69 W/(m K), the $Y$-component ($b$ direction) the highest 2.49 W/(m K), and the $Z$-component ($c$ direction) an intermediate value of 1.99 W/(m K). It is noted that these individual values are high compared with the experimental data presented in Fig. 7d, but we stress that it is the relative differences and not the absolute values that are most instructive at this stage. A detailed simulation investigation, including different compositions and temperatures, is ongoing and will be reported elsewhere.

The figure of merit for composition X27 is shown in Fig. 8. It increases linearly with temperature, peaking at 750°C with a value of about 0.16. Although this value is comparable to $ZT$ values for $p$-type cobaltite oxides, we believe that, with control of texture and improvement of the electrical

conductivity (perhaps by introduction of a conductive phase into the ceramic), higher values of $ZT$ can be achieved.

## CONCLUSIONS

$Ba_{6-3x}Nd_{8+2x}Ti_{18}O_{54}$ tungsten-bronze-structure ceramics exhibit stable, anisotropic, low values of thermal conductivity, with high Seebeck coefficient and moderate electrical conductivity. The first assessment of the thermoelectric properties suggests that $Ba_{6-3x}Nd_{8+2x}Ti_{18}O_{54}$ tungsten bronze can be considered a potential candidate for high-temperature applications.

## ACKNOWLEDGEMENTS

## OPEN ACCESS

## REFERENCES

1. D.M. Rowe, *Renew. Energy* 16, 1251 (1999).
2. K. Koumoto, R. Funahashi, E. Gilmeau, Y. Miyazaki, A. Weidenkaff, Y. Wang, and C. Wen, *J. Am. Ceram. Soc.* 95, 1 (2012).
3. T. Okuda, K. Nakanishi, S. Miyasaka, and Y. Tokura, *Phys. Rev. B* 63, 113104 (2001).
4. S. Ohta, T. Nimura, H. Ohta, and K. Koumoto, *J. Appl. Phys.* 97, 034106 (2005).
5. C.Y. Gao, H.R. Xia, J.Q. Xu, C.L. Zhou, H.J. Zhang, and J.Y. Wang, *Appl. Phys. Lett.* 92, 231905 (2008).
6. S. Lee, R.H.T. Wilke, S. Trolier-McKinstry, S. Zhang, and C.A. Randall, *Appl. Phys. Lett.* 96, 031910 (2010).
7. L. Yi, L. Jian, W. Chun-Lei, S. Wen-Bin, Z. Yuan-hu, L. Ji-Chao, and M. Liang-Mo, *Chin. Phys. B* 24, 047201 (2015).
8. H. Ohsato, T. Ohhashi, S. Nishigaki, T. Okuda, K. Sumiya, and S. Susuki, *Jpn. Appl. Phys.* 32, 4323 (1993).
9. M. Valant, D. Suvorov, and D. Kolar, *J. Mater. Res.* 11, 928 (1996).
10. C.C. Tang, M.A. Roberts, F. Azough, C. Leach, and R. Freer, *J. Mater. Res.* 17, 675 (2002).
11. H. Ohsato and M. Imaeda, *Mater. Chem. Phys.* 79, 208 (2003).
12. S. Plimpton, *J. Comput. Phys.* 117, 1 (1995).
13. P. Canepa, PhD Thesis University of Kent (2012), http://ethos.bl.uk/OrderDetails.do?did=1&uin=uk.bl.ethos.580391.
14. M.S. Green, *J. Chem. Phys.* 22, 398 (1954).
15. R. Kubo, *J. Phys. Soc. Jpn.* 12, 570 (1957).
16. H. Ohsato, T. Ohhashi, S. Nishigaki, and T. Okuda, *Jpn. J. Appl. Phys.* 32, 4323 (1993).
17. W. Tian and R. Yang, *CMES* 24, 123 (2008).
18. G. Li, J. Yang, Y. Xiao, L. Fu, M. Liu, and J. Peng, *J. Am. Ceram. Soc.* 96, 2703 (2013).
19. H. Okudera, H. Nakamura, H. Toraya, and H. Ohsat, *J. Solid State Chem.* 142, 336 (1999).